Materials and Design 181 (2019) 108064

Contents lists available at ScienceDirect

Materials and Design

journal homepage: www.elsevier.com/locate/matdes

Beta-type Ti-Nb-Zr-Cr alloys with large plasticity and significant strain hardening

S.F. Jawed [a], C.D. Rabadia [a], Y.J. Liu [b], L.Q. Wang [c,*], Y.H. Li [d], X.H. Zhang [d], L.C. Zhang [a,*]

[a] School of Engineering, Edith Cowan University, 270 Joondalup Drive, Joondalup, Perth, WA 6027, Australia
[b] School of Engineering, The University of Western Australia, 35 Stirling Highway, Perth, WA 6009, Australia
[c] State Key Laboratory of Metal Matrix Composites, School of Material Science and Engineering, Shanghai Jiao Tong University, No. 800 Dongchuan Road, Shanghai 200240, China
[d] School of Mechanical Engineering, Xi'an University of Science and Technology, Xi'an 710054, China

HIGHLIGHTS

- The microstructures of Ti-25Nb-8Zr-xCr alloys are affected by Cr addition.
- Both yield strength and hardness increase due to solid-solution strengthening effect.
- The content of Cr substantially enhances plasticity and strain hardening rate.
- Deformation mechanisms predicted by $\overline{Bo}$-$\overline{Md}$ diagram are in line with that by $\overline{e/a}$-$\overline{\Delta r}$ diagram for the studied alloys.

GRAPHICAL ABSTRACT

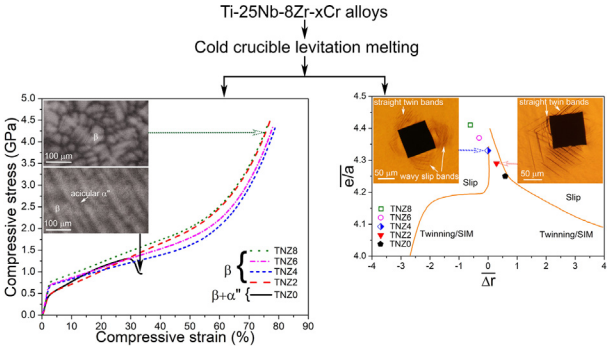

ARTICLE INFO

Article history:
Received 8 April 2019
Received in revised form 1 July 2019
Accepted 19 July 2019
Available online 20 July 2019

Keywords:
Titanium alloy
Plasticity
Strength
Strain hardening
Deformation band
Shear band

ABSTRACT

A series of Ti-25Nb-8Zr-xCr (x = 0, 2, 4, 6, 8 wt%) alloys were designed based on DV-Xα cluster method and $\overline{e/a}$-$\overline{\Delta r}$ diagram with an anticipation to obtain high plasticity and significant strain hardening. The designed alloys were produced through cold crucible levitation melting technique in order to effectively investigate their microstructures and mechanical properties. The addition of Cr significantly enhances the β stability in the microstructures of the Ti-25Nb-8Zr-xCr alloys. Both yield strength and hardness of the studied alloys increase due to the effect of solid-solution strengthening. By constrast, the plasticity, maximum strength and strain hardening rate are influenced by the β stability as well as the distinct deformation mechanisms. None of the alloys comprising Cr fail up to 100 kN (the load capacity used) and all show impressive plasticity (~75%) and superior maximum compressive strength (~4.5 GPa) at 100 kN. Moreover, the deformation bands, which are found around the hardness indentations, are analyzed for all the investigated alloys. The fracture behaviors of the Ti-25Nb-8Zr-xCr alloys are also studied to observe the characteristics related to crack propagation, plastic deformation and the formation of shear bands.

1. Introduction

Titanium (Ti) alloys have been extensively used in industries ranged from the fields of aerospace to biomedical engineering where they have

* Corresponding authors.
E-mail addresses: wang_liqiang@sjtu.edu.cn (L.Q. Wang), l.zhang@ecu.edu.au, lczhangimr@gmail.com (L.C. Zhang).

https://doi.org/10.1016/j.matdes.2019.108064

been employed due to their unique performance of high strength, low Young's modulus, superior plasticity, high density, enhanced formability, high corrosion resistance and low bio-toxicity [1–3]. Among the previously investigated alloys, β type Ti alloys have explicitly received more attention due to their balanced combination of mechanical properties [4–6]. Presently, the conventional metallic alloys such as stainless steel, cobalt-chromium (Co-Cr), commercially pure Ti and Ti-6Al-4V are being used in the field of biomedical implants; nonetheless these alloys have some limitations such as bio-incompatibility, high stiffness, high toxicity, and poor corrosion resistance behavior [7,8]. The so-called "stress shielding" phenomenon is prominent in these conventional biomaterials where the stiffness of these biomaterials is higher than that of the surrounding bone tissue [9–11]. This has necessitated the development of improved biomedical implant materials [12]. Primarily, an improved β phase stability is important in designing Ti alloys with enhanced properties to overcome the stress shielding issue [13,14]. β Ti alloys have lower stiffness than that of other multi-phase Ti alloys because β Ti alloys possess body-centerd cubic (bcc) crystalline structure [15]. Furthermore, the effective cold forming attribute of β Ti alloys minimizes their manufacturing cost [16]. Metastable β Ti alloys persistently show an effective balance between strength and ductility through the variation of different deformation mechanisms, such as mechanical twinning, stress-induced martensite (SIM) and dislocation slip as a function of β phase stability [17,18]. The phenomena of mechanical twinning and/or SIM transformation induce large ductility through high strain hardening rate and low yield strength, whereas the dislocations slip impels lower elongation and high yield strength [19,20]. Adequate amount of β stabilizing elements (e.g. Nb, Ta, Mo, Mn, Fe, Cr) enhance the β stability of Ti alloys [21,22]. Therefore, the selection of alloying elements and their quantities are certainly important in the development of enhanced Ti alloys.

In the last decade, considerable endeavors have been made to develop new β Ti alloys with reduced Young's modulus and enhanced superelasticity for biomedical implant applications. Nonetheless, the β Ti alloys, which have been developed until now, have demonstrated poor ductility and insufficient strain hardening as compared to Co-Cr alloys and stainless steel. These drawbacks restrict their use in advanced applications where an effective combination of ductility and strength is required [23]. Currently, researchers are focusing on designing a new family of Ti alloys comprising the combination of enhanced ductility and significant rate of strain hardening [24,25]. Morinaga et al. [26–28] have originally formulated the DV-Xα strategy for estimating the stability of β phase in Ti alloys. However, many researchers have used this DV-Xα design principle to develop new metastable β Ti alloys having simultaneous SIM and twinning deformation mechanisms [17]. Although the number of β Ti alloys have been developed through DV-Xα cluster method with the compositions to be spotted on the twinning/SIM region in $\overline{Bo}$-$\overline{Md}$ diagram ($\overline{Bo}$: the average bond order; $\overline{Md}$: the average *d*-orbital energy level (*Md*)) and those alloys have also confirmed the actual formation of twinning/SIM mechanisms [19]. Nonetheless, some discrepancies between the spotted location of an alloy in $\overline{Bo}$-$\overline{Md}$ map and actual deformation mechanism obtained have also been reported [19]. A new predictive approach has recently been developed for the prediction of different deformation mechanisms of β-Ti alloys [19,29]. Therefore, the aforementioned theoretical design approaches have been used in this work to estimate the β phase stability and compare the various deformation mechanisms.

In pursuit of resolution to the strength-ductility trade-off dilemma in Ti alloys, the optimal combination of elements for designing quaternary group of Ti alloys was selected in this work. In order to attain an improved combination of optimal mechanical properties, niobium (Nb), chromium (Cr) and zirconium (Zr) have been selected in this work from β-isomorphous, β-eutectoid and neutral elements, respectively. Nb in Ti alloys shows superior traits such as effective shape memory and superelastic behavior, low Young's modulus, high biocompatibility and corrosion resistance, which are some essentials for biomedical applications [8]. According to some reported studies, the content of Nb in Ti alloys reduces its elastic modulus and increases the β stability [30]. Zr typically resides in the same group with Ti and the content of Zr suppresses the martensitic transformation in β Ti alloys with minimum variation in the lattice deformation strain [31,32]. The quantities of Zr close to 8 wt% completely suppress the formation of ω phase in Ti alloys [33]. Cr has been selected as one of the alloying elements because it is a low-cost strong β stabilizer. Cr also regulates the anodic activity of Ti and also increases its propensity to passivate, thereby enhancing corrosion resistance of Ti [34,35]. Furthermore, the addition of Cr as an alloying element suppresses the formation of athermal ω phase in Ti alloys [8]. Gao et al. [36] reported that Ti-Cr alloys possess the effect of twin-induced plasticity, resulting in large elongation and increased yield strength. Li et al. [37] alloyed Cr with Ti–29Nb–13Ta–4.6Zr to reduce its springback via deformation induced ω transformation.

In this work, the Ti-25Nb-8Zr-xCr (x = 0, 2, 4, 6, 8 wt%) alloys were initially designed on the basis of $\overline{e/a}$-$\overline{\Delta r}$ diagram and DV-Xα cluster method [19,26]. Further, molybdenum equivalent (Mo_{eq}) has also been taken into consideration when designing the novel Ti-25Nb-8Zr-xCr alloys. To the best of our knowledge, the effects of Cr content on mechanical properties and microstructures of Ti-Nb-Zr alloys have not yet been evaluated. Thus, this work systematically investigates the microstructure, mechanical properties and deformation behavior of the Ti-25Nb-8Zr-xCr alloys, with the variation in the quantities of Cr from 0 wt% to 8 wt%. Moreover, the deformation bands observed around Vickers indentions of the Ti-25Nb-8Zr-xCr alloys have also been analyzed.

2. Materials and methods

The Ti-25Nb-8Zr-xCr (x = 0, 2, 4, 6, 8 wt%) alloys are hereafter shortened as TNZx (where x is the weight percent of Cr). For instance, Ti-25Nb-8Zr was shortened as TNZ0, Ti-25Nb-8Zr-8Cr was shortened as TNZ8, and so on.

2.1. Rationale theoretical design for the novel Ti alloys

The TNZx alloys were theoretically designed on the basis of approach established by Morinaga et al. [26] known as DV-Xα cluster strategy which is widely used to predict β phase stability and deformation mechanism for the designed Ti alloys based on the two electronic parameters [38] i.e. the bond order (*Bo*) and the *d*-orbital energy level (*Md*) [28]. *Bo* represents the overlap population between the atomic orbitals of parent element and alloying elements [39]. The overlap population is in proportional relationship with covalent bond strength between a parent element and other alloying elements [39]. Whereas, *Md* correlates the atomic radius and electronegativity of alloying elements [8]. *Md* remains in proportional relationship with atomic radius of an element, while it remains in inverse relationship with electronegativity of an element [39]. The average values of $\overline{Bo}$ and $\overline{Md}$ for the TNZx alloys were evaluated by the respective formulae suggested in Ref. [40]. Additionally, a new semi-empirical approach developed by Wang et al. [19] was used to design novel group of TNZx alloys. This approach was developed on the basis of two parameters, i.e. the valence electron concentration (e/a) and the atomic size difference (Δr). This approach involves plotting of their compositional average on $\overline{e/a}$-$\overline{\Delta r}$ diagram [19]. The values of $\overline{e/a}$ and $\overline{\Delta r}$ for the Ti-25Nb-8Zr-xCr alloys were estimated using the Eqs. (1) and (2) [19].

$$\overline{\Delta r} = \sum_i^n c_i(r_i - r_{\overline{n}}) \quad (1)$$

$$\overline{e/a} = \sum_i^n c_i e_i \quad (2)$$

where c_i, r_i and e_i are the atomic fraction, atomic radius and valence electron number of the ith atom, respectively. Mo_{eq} is also a significant parameter for theoretically ensuring the β phase stability and estimating various deformation mechanisms. Mo_{eq} can be calculated using the equation of Mo_{eq} suggested in Ref. [7]. The calculated-values of $\overline{Bo}$, $\overline{Md}$, $\overline{e/a}$, $\overline{\Delta r}$ and Mo_{eq} for the TNZx alloys are summarized in Table 1.

2.2. Experimental procedure

The TNZx alloys were manufactured from the mixtures of 99.9% pure Ti, Nb, Cr and Zr metals through cold crucible levitation melting (CCLM) method under an argon atmosphere. The CCLM furnace is a kind of induction melting furnace consists of water cooled crucible, which is made from high purity cooper segments. Ti is chemically reactive in molten form, consequently, at higher temperatures this trait leads to the problem of inhomogeneity [12]. In order to obtain the homogeneity in chemical compositions, CCLM furnace uses electromagnetic force for producing diffusion mixing with strong stirring that can effectually melt alloying elements without any inhomogeneity and contamination [41,42]. After strong mixing and melting, rapid quenching of each alloy was carried out in the water-cooled copper crucible. The investigated alloys were cast in the form of ingots rather than directly cast in the form of cylindrical bars. As such, cylindrical rods with 5.3 mm in diameter were prepared for each alloy using wire electrical discharge machining from the core of the corresponding cast ingot for all the type of analyses presented in this work. Therefore, cooling effect does not affect the microstructure as the cylindrical rods were taken from core of the ingots. On the other hand, the length of approximately 5 mm at the top and bottom of the cylindrical rods were also not used in all the types of analyses presented in this work. After taking out the cylindrical rods from ingots, the cylindrical rods were cut using a Buehler Isomet 1000 to obtain several specimens for the analyses of microstructures, phase characterization and mechanical properties.

The microstructural investigations of the TNZx alloys were characterized by performing scanning electron microscopy (SEM) for capturing microstructural images using a FEI verios XHR 460 microscope. Prior to microstructural investigations, all the specimens were ground using silicon carbide papers up to 2000 grits and subsequently specimens were polished using a suspension liquid of Struers OP-S colloidal silica on a Struers MD-Chem polishing pad. Later, specimens were cleaned using an ultrasonic cleaner and finally the Kroll's reagent (30 vol% nitric acid, 5 vol% hydrofluoric acid and 65 vol% water) was used to etch the surface of specimens. The quantitative analysis for all the investigated compositions was performed from energy dispersive X-ray spectroscopy (EDX). The oxygen contents on multiple samples of each alloy (about 0.1 g after cleaning) were obtained for all the investigated TNZx alloys by hot gas extraction followed by mass spectrometry using a LECO Analyzer ONH 836.

The phase characterization in the TNZx alloys were carried out by X-ray diffraction (XRD) using a PANalytical EMPYREAN diffractometer operated at 40 kV and 40 mA with a Co-kα radiation (λ = 0.1789 nm). The XRD profile of each alloy was acquired in a 2θ range from 30° to 110° at a scan rate of 0.011°/s with a step size of 0.013°. The lattice parameter of bcc β phase (α_β) was evaluated using the Bragg's formula (Eq. (3)) [8]:

$$a = \frac{\lambda\sqrt{h^2 + k^2 + l^2}}{2\ \sin\theta} \quad (3)$$

where λ is wavelength, (h, k, l) are the miller indices of the diffraction planes and θ is the Bragg angle.

Further, the precised α_β for TNZx alloys was estimated using Nelson-Riley's extrapolation function i.e. $((\cos^2\theta/\sin\theta) + (\cos^2\theta/\theta))$ [8]. Structural and phase information were characterized using JCPDS powder diffraction files.

The analyses of mechanical properties were carried out using uniaxial compression and Vickers micro-hardness testing. Cylindrical specimens were prepared by grinding both facets to keep them flat and maintaining the length to diameter ratio of around 1.8 as per ASTM E9 standard. Three compression tests for all the TNZx alloys were performed at ambient temperature on prepared cylindrical specimens at a cross head speed of 0.1 mm/min using an Instron 5982 universal testing machine having 100 kN load capacity. The 0.2% offset method was used to estimate compressive yield strength from engineering stress-strain curves. The values of true stress and true strain for the TNZx alloys were evaluated from engineering stress and engineering strain for compressed specimens using the equations mentioned in Ref. [43]. Further, the rate of strain hardening for each alloy was evaluated using the Eq. (4) [44].

$$\theta = \frac{\partial\sigma_T}{\partial\varepsilon_P} \quad (4)$$

where $\partial\sigma_T$ is true stress and $\partial\varepsilon_P$ is true plastic strain.

Fracture analyses were performed on the specimens undergone the compression tests. FEI Verios XHR 460 scanning electron microscope was used to get information about deformation, crack features and shear band formations. Vickers micro-hardness were performed on polished samples of the TNZx alloys using Zwick Roell ZHU micro-hardness tester. Ten indentations were taken at different places covering the maximum surface area of the specimen with a dwell time of 30 s and at a load of 5 kgf. To investigate the elasto-plastic deformation mechanisms, Zeiss Axiocam optical microscope was used.

3. Results and discussion

Table 2 presents the quantities of alloying elements present in the alloy compositions (in wt%) and the oxygen content (in wt%) present in all the as-cast Ti-25Nb-8Zr-xCr alloys. The results of nominal and measured chemical compositions are almost identical, with the minimal amount of oxygen content found for all the TNZx alloys.

3.1. Microstructure and phase analyses

Fig. 1 presents the XRD profiles of the TNZx alloys. The TNZ0 alloy comprises the orthorhombic α″ and bcc β phases, whereas the Cr-containing alloys, i.e. TNZ2, TNZ4, TNZ6 and TNZ8, contain only bcc β

Table 1
The values of $\overline{Bo}$, $\overline{Md}$, $\overline{e/a}$, $\overline{\Delta r}$ (Å) and Mo_{eq} (wt%) for all the as-cast Ti-25Nb-8Zr-xCr alloys.

Alloys	Chemical composition (wt%)	$\overline{Bo}$	$\overline{Md}$	$\overline{e/a}$	$\overline{\Delta r}$	Mo_{eq}
TNZ0	Ti-25Nb-8Zr	2.8521	2.4677	4.25	0.59	6.9
TNZ2	Ti-25Nb-8Zr-2Cr	2.8519	2.4465	4.29	0.29	9.4
TNZ4	Ti-25Nb-8Zr-4Cr	2.8518	2.4252	4.33	−0.01	11.9
TNZ6	Ti-25Nb-8Zr-6Cr	2.8517	2.4038	4.37	−0.31	14.4
TNZ8	Ti-25Nb-8Zr-8Cr	2.8516	2.3824	4.41	−0.61	16.9

Table 2
The quantities of alloying elements (in wt%) and the oxygen content (in wt%) present in the as-cast Ti-25Nb-8Zr-xCr alloys.

Alloys	Chemical composition (wt%)	Ti (wt%)	Nb (wt%)	Zr (wt%)	Cr (wt%)	O (wt%)
TNZ0	Ti-25Nb-8Zr	Bal.	26.2 ± 3.0	8.2 ± 1.2	0.0 ± 0.0	0.0794 ± 0.0003
TNZ2	Ti-25Nb-8Zr-2Cr	Bal.	24.9 ± 1.2	8.4 ± 0.7	2.3 ± 0.2	0.0902 ± 0.0003
TNZ4	Ti-25Nb-8Zr-4Cr	Bal.	25.1 ± 1.9	9.2 ± 1.6	4.7 ± 0.6	0.0935 ± 0.0017
TNZ6	Ti-25Nb-8Zr-6Cr	Bal.	25.7 ± 1.8	7.9 ± 0.9	6.0 ± 0.4	0.1065 ± 0.0022
TNZ8	Ti-25Nb-8Zr-8Cr	Bal.	24.2 ± 3.0	8.2 ± 1.8	8.1 ± 0.9	0.0904 ± 0.0003

phase. The diffraction peaks of bcc Cr-containing Ti alloys shift towards higher 2θ angles upon increasing the Cr content. This is evident due to smaller atomic radius of Cr as compared to Ti [41]. The calculated α_β values for TNZ0, TNZ2, TNZ4, TNZ6 and TNZ8 are found to be 0.3307, 0.3293, 0.3283, 0.3274 and 0.3264 nm respectively. The α_β of bcc Ti alloys comprising Cr reduces as content of Cr increases in the as-cast alloys because the atomic radius of Cr is smaller than Ti [41]. The α_β of TNZ0 alloy is 0.3307 nm which is slightly higher than that of standard bcc Ti (0.3306 nm) due to presence of Zr as it has higher atomic radius as compared to Ti [45,46]. The orthorhombic α″ is found in the TNZ0 alloys because of martensitic transformation which occurs after rapid quenching [47,48]. The cooling rate plays a significant role in phase transformation from β → α″ phase when alloys solidify from high temperature [49]. It was widely reported that, after rapid quenching of Ti alloys, β phase may transform into different phases, i.e. α″, α′, α and ω phases [15,49]. It can be noticed that only bcc β peaks are evident on the XRD profiles of the as-cast Cr-containing alloys. It is well known that Cr is a strong β stabilizer [8,50] and therefore, it substantially enhances the β stability by adding only 2% of Cr in the TNZx alloys. It was reported that the existence of ω phase (Space group: P6/mmm, PDF card no: 00-051-0631) can be detected by XRD at low scanning speed of 0.5°/min [11,34]. Accordingly, the XRD curves of the TNZx alloys acquired at slow scan speed of 0.011°/s with a step size of 0.013° in this work, which could also detect the ω phase if it exists in the studied alloys. According to PDF card no: 00-051-0631, ω phase is associated with the XRD peaks having hkl = 001, 111, 002, 112. In the present work, none of the aforementioned XRD peaks are found for the investigated alloys. Therefore, ω phase is not expected or has trace amount in all the investigated TNZx alloys.

The microstructure images of the TNZx alloys are shown in Fig. 2. Only the TNZ0 represents the two phases, i.e. bcc β and orthorhombic α″ phases, whereas the Cr-containing TNZx alloys, i.e. TNZ2, TNZ4, TNZ6 and TNZ8 predominantly constitute the full β phase. Therefore, β is a leading phase in the microstructures of all the TNZx alloys. Moreover, an equiaxed structure of the bcc β phase can be clearly observed with the β grain boundaries in the SEM images of all the TNZx alloys. Further, the dendritic substructure, which usually occurs during solidification [51], can also be visible inside the β equiaxed grains in all the studied alloys. It can be noted that, the two kind of contrast happen in Fig. 2b–e for TNZ2, TNZ4, TNZ6 and TNZ8 respectively due to dendritic sub-structure which is present inside the β grains. By constrast, in Fig. 2a, needles of α″ phase are also evident in the microstructure along with the contrast effect produced by dendritic sub-structure of the β grains. The evident peaks related to α″ phase are also found in the XRD profile of TNZ0. A high-magnification BSE inset image has been placed in Fig. 2a to clearly show the acicular structure of α″ phase. Based on the results of microstructure and phase characterization, TNZ0 contains dual phase, i.e. β and α″ phases, while the remaining alloys (TNZ2, TNZ4, TNZ6 and TNZ8) contain single β phase. Moreover, EDX mapping results (not shown herein) show that the Cr has homogeneously distributed in the alloys for all the investigated alloys.

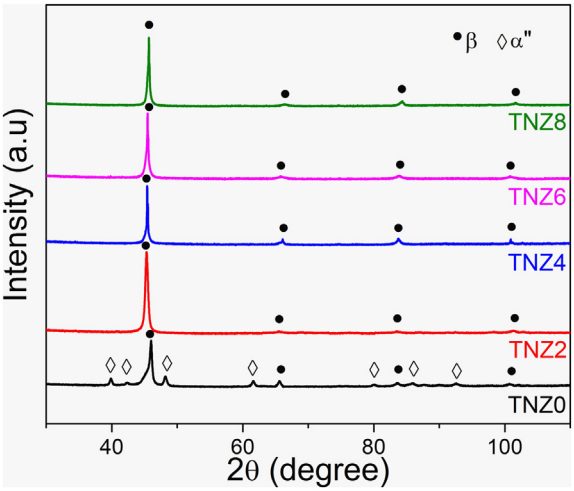

Fig. 1. The XRD patterns of the Ti-25Nb-8Zr-xCr alloys (the alloys are shortened as TNZx).

3.2. Mechanical properties

It is known that the microstructural characteristics and their corresponding V_f constitutes in Ti alloys influence their mechanical properties [15,52]. Therefore, to investigate the influence of different compositions on the mechanical performance of the designed Ti alloys, compression testing at room temperature and Vickers micro-hardness tests were conducted.

Fig. 3 demonstrates the compressive engineering stress-strain curves taken for the TNZx alloys at room temperature. The stopping criterion for the compressive tests was either the alloy failed or when the compression testing machine reached 100 kN (the load capacity of the mechanical machine). It can be noticed from Fig. 3 that all the studied TNZx alloys except for the TNZ0 exhibit very large plastic strain and do not fail until the 100 kN is reached. Note that, the addition of Cr significantly enhances the mechanical properties (strength and plasticity) of the TNZx alloys. Fig. 3 inset shows the difference in specimen-size before and after compression testing for TNZ8. A small shear crack (after the compression test) on the specimen-surface of TNZ8 can also be seen in Fig. 3 inset because the definite fracture has not occurred in any Cr-containing TNZx alloys, until the load reaches 100 kN in compression testing.

Fig. 4 shows the relationship between yield strength ($\sigma_{0.2}$) and Hardness (H) of the TNZx alloys. In this work, both $\sigma_{0.2}$ and H change in a same fashion as both have a proportional relationship with each other [8,53,54]. It is clear from Fig. 4 that the values of $\sigma_{0.2}$ and H increase gradually with increasing the Cr content in the studied alloys. The values of $\sigma_{0.2}$ for the Cr-containing alloys vary from 385 ± 44 MPa to 773 ± 28 MPa. Further, the values of H for the Cr-containing alloys vary from 1.94 ± 0.05 GPa to 2.63 ± 0.06 GPa. Such an increasing trend of $\sigma_{0.2}$ and H for the TNZx alloys is positively influenced by the effect of solid-solution strengthening [55]. The phenomenon of solid-solution strengthening occurs as per the well-known Hume-Rothery rule due to adding low atomic radius (solute) element, i.e. Cr in the investigated alloys [41].

It is of worth noting from Fig. 5 that the addition of Cr significantly enhances the plastic strain and maximum compressive strength obtained at 100 kN for all the studied alloys. Among the investigated alloys, TNZ0 exhibits the lowest plastic strain (28 ± 0.5%) as it consists

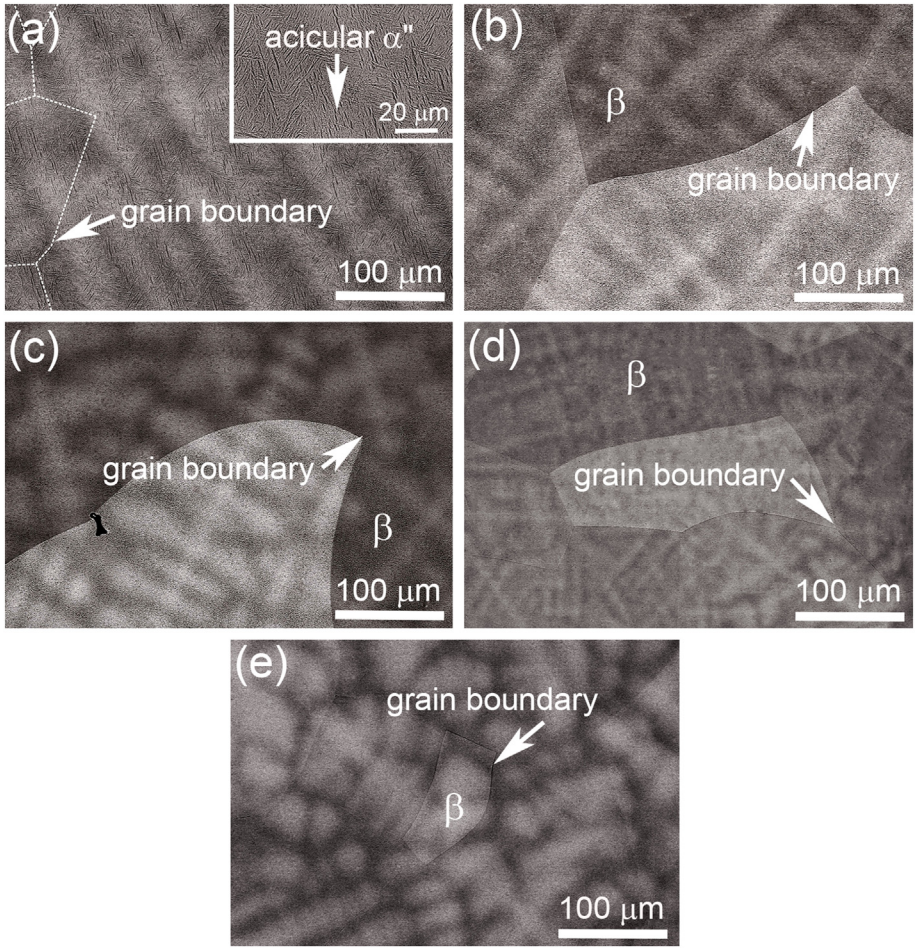

Fig. 2. The backscattered SEM microstructure images of the Ti-25Nb-8Zr-xCr alloys: (a) 0 wt%, (b) 2 wt%, (c) 4 wt%, (d) 6 wt% and (e) 8 wt%.

of α″ phase along with β phase. Whereas, all the Cr-containing alloys display superior plastic strain (~75%) and maximum compressive strength (~4.5 GPa) at 100 kN, because the Cr has enhanced the β phase stability and thus suppresses the α″. Accordingly the mechanical properties (both strength and plasticity) of all the investigated Cr-containing TNZx alloys are significantly enhanced [15]. In the present work, the mechanical properties are influenced by the addition of Cr. Moreover, all the investigated alloys show equiaxed β grains and the size of the β grains decrease as the content of Cr increases in the TNZx alloys. However, it is difficult to measure the accurate average size of the β grains as the size of the β grains is greater than around 300–500 μm in all the investigated alloys. It can be inferred based on the points discussed above that the mechanical properties are affected due to the content of solute element (i.e. Cr) and due to the effect of grain boundary strengthening. This shows that difference in dendritic structure do

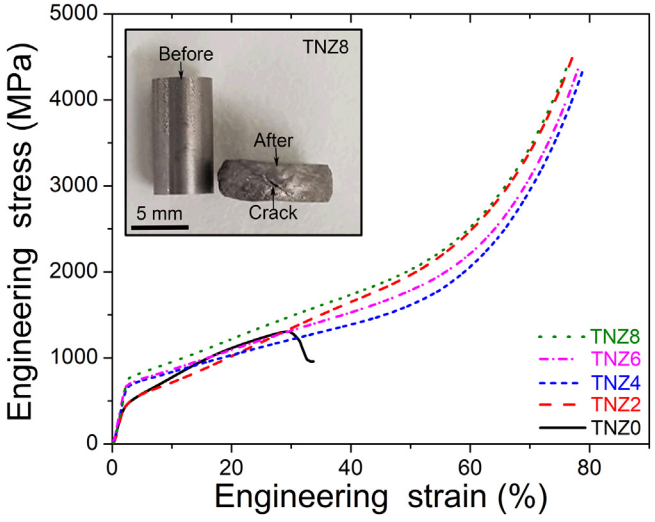

Fig. 3. The ambient temperature engineering stress-strain curves of the Ti-25Nb-8Zr-xCr alloys (the alloys are shortened as TNZx).

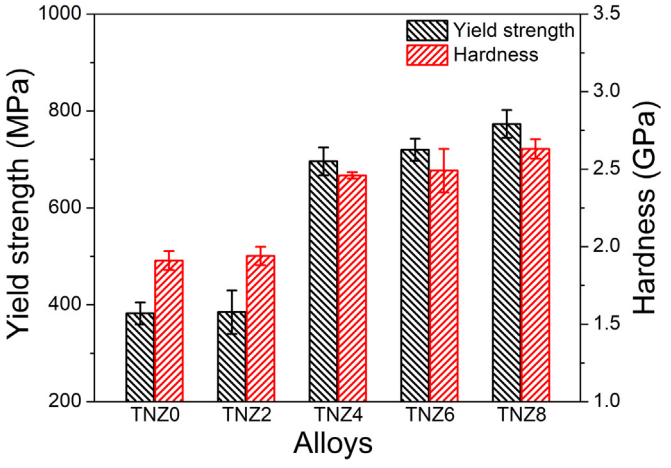

Fig. 4. Yield strength ($\sigma_{0.2}$) and hardness (H) of the Ti-25Nb-8Zr-xCr alloys (the alloys are shortened as TNZx).

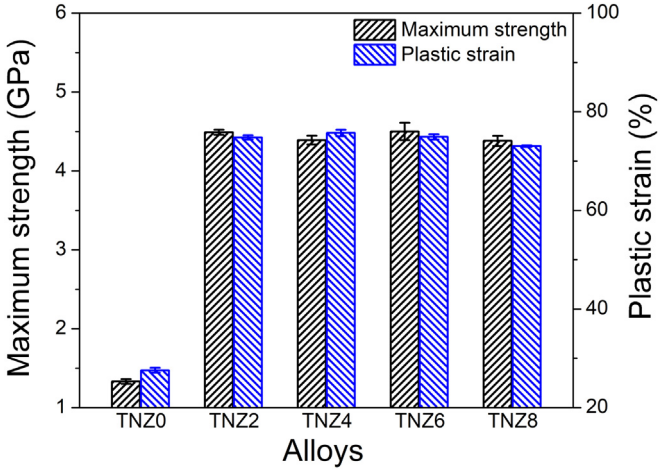

Fig. 5. Maximum strength (σ_{max}) and plastic strain (e_p) of the Ti-25Nb-8Zr-xCr alloys (the alloys are shortened as TNZx).

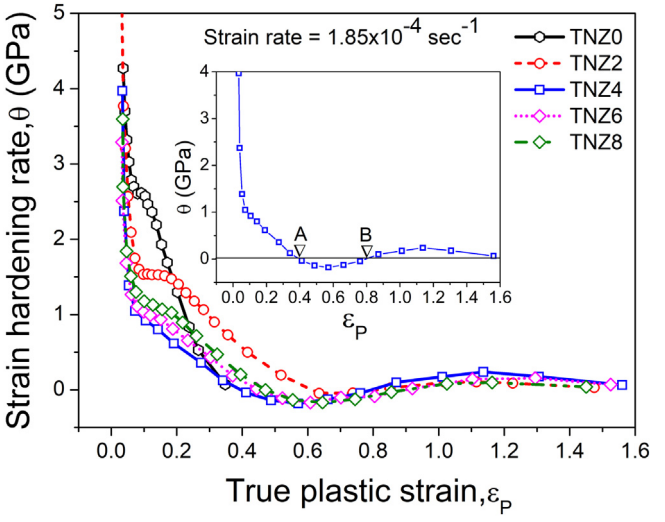

Fig. 7. The strain hardening rate as a function of true plastic strain of the Ti-25Nb-8Zr-xCr alloys (the alloys are shortened as TNZx). Inset shows the variation in strain hardening stages.

not contribute in the variation of mechanical properties for all the investigated alloys.

Fig. 6 presents the compressive true stress-strain curves obtained at room temperature for the TNZx alloys. It can be observed from Fig. 6 that the true stress-strain curves comprise multiple peaks of stress oscillations and these curves include four stages: (I) elastic stage, (II) first strain hardening stage, (III) strain softening stage and (IV) second strain hardening stage as presented in Fig. 6 inset only for TNZ4 as an example to show the four stages. Such kind of multiple-peak oscillations have also been reported in the previous work on Ti-Nb-Ta-Zr-O alloy during straining [56]. The first strain hardening stage occurs based on the dynamic Hall-Petch effect, which shows that α″ martensite and twinning deformation produce new sharp interfaces due to continuous subgrain division. These interfaces would also restrict the dislocation motion and minimize the dislocation mean free path, thereby causing increased rate of strain hardening [57,58]. The strain softening is produced due to the effect of stress relaxation in which stress intensity reduces when the specimen is loaded for quite long period of time at constant strain rate [59]. Second strain hardening stage occurs due to the formation of shear bands [56,60]. As such, at the end of compression test, a high intensity of shear stress remains in the specimen and the deformation mechanism alters into the formation of shear bands [56].

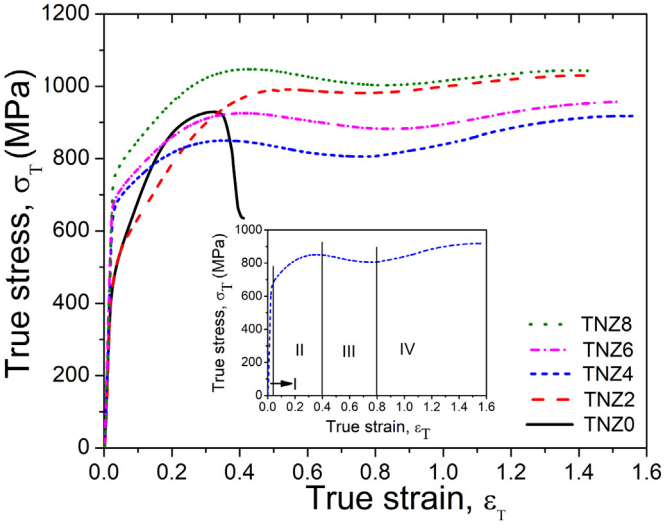

Fig. 6. The true stress-strain curves of the Ti-25Nb-8Zr-xCr alloys (the alloys are shortened as TNZx). Inset shows the four stages in deformation.

Fig. 7 illustrates the relationship between strain hardening rate (θ) and true plastic strain (ε_p) for the TNZx alloys. The inset presented in Fig. 7 is for TNZ4 only as an example to show the variation in θ. The $\partial\sigma_T/\partial\varepsilon_p$ for TNZx alloys containing Cr comprises, the first strain hardening stage (before point A), the strain softening stage (between points A and B) and the second strain hardening stage (after point B). It is clear from inset Fig. 7 that $\partial\sigma_T/\partial\varepsilon_p < 0$ during strain softening stage, $\partial\sigma_T/\partial\varepsilon_p > 0$ during strain hardening stages and $\partial\sigma_T/\partial\varepsilon_p \approx 0$ at points A and B. Notably, the θ increases by adding 2 wt% Cr in the TNZ0 alloy (i.e. the TNZ2 alloy) (5 GPa) during first stage of strain hardening. This occurs due to the activation of twin deformation mechanism [36,61,62]. The second strain hardening stage occurs due to the formation of shear bands. Therefore, TNZ4 demonstrates the highest rate of strain hardening (0.65 GPa) in the second stage among the investigated TNZx alloys because the highest plasticity is also found in TNZ4 among all the studied alloys [56].

3.3. The elasto-plastic deformation

The elasto-plastic deformation behavior can be analyzed effectively by studying the deformation patterns around the Vickers indentation [62]. Typically, there are three forms of morphologies formed around micro-hardness indentations of an alloy (i.e. “Sink-in”, “pile-up” and “crack”) [53]. The formation of deformation bands, extrusion and cracks may occur during hardness testing around the impression of an indenter [53]. While performing indentation in hardness testing, the deformation of material around the edge of an indenter takes place due to both the shear and normal stress components, whereas the deformation around the corners emerges because of normal stress components only which remains the cause of crack formation [53]. The wavy and straight morphologies of deformation bands around the hardness indentation can be used to determine the boundaries between slip and twin mechanism in $\overline{Bo}$-$\overline{Md}$ map [39]. Wavy slip bands form around indentation when slip mechanism is dominant and straight twin bands form around indentation when twin mechanism dominates the deformation of a material [39].

Fig. 8 displays the optical micrographs which were captured around the micro-hardness indentations of the TNZx alloys. No crack morphology is found on the corners of an indenter for all the investigated alloys as all show significant plasticity in compressive testing as shown in Fig. 6. Hence, few deformation bands are obtained around the hardness indentation for TNZ0 (Fig. 8a), because

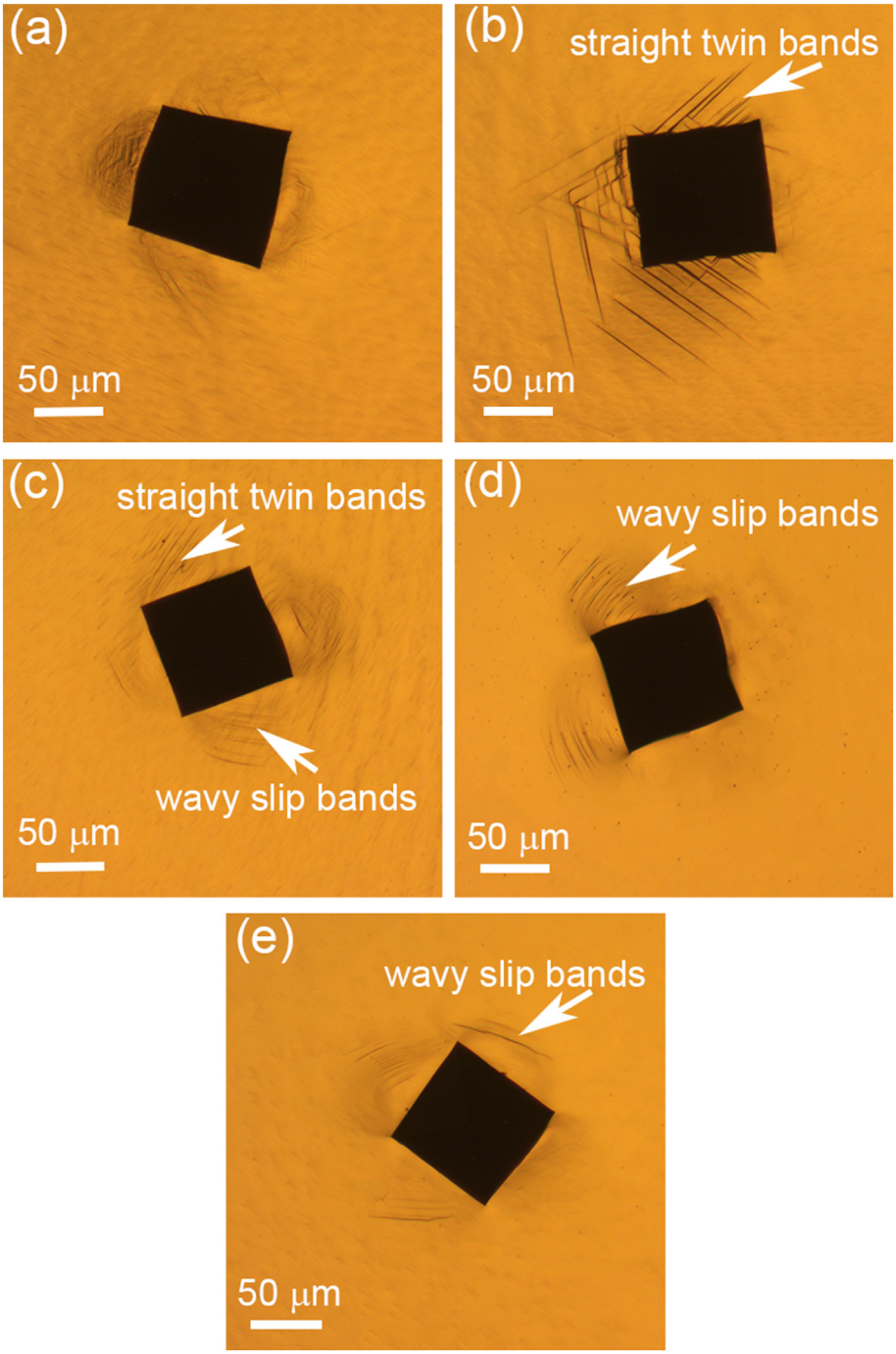

Fig. 8. The optical micrographs around the Vickers micro-hardness indentations captured for the Ti-25Nb-8Zr-xCr alloys (the alloys are shortened as TNZx): (a) TNZ0, (b) TNZ2, (c) TNZ4, (d) TNZ6 and (e) TNZ8.

it has the lowest plastic deformation strain among the investigated alloys. A substantial increase in the number of bands can be clearly observed from Fig. 8b after addition of 2 wt% Cr in the TNZ0 alloy. As such, the morphology of the bands around the indentations of TNZ2 is straight twin, which represents that twin mechanism is dominant in the deformation of TNZ2 alloy [39]. In Fig. 8c, more wavy slip bands are observed along with a few straight twin bands, which represents the activation of twin + slip deformation mechanism in the TNZ4 alloy [39]. It can be clearly seen from Fig. 8d–e that only wavy slip bands are formed around the indentations, which indicates that slip mechanism is dominant in the defamation of both TNZ6 and TNZ8 alloys [39].

Figs. 9 and 10 shows the boundaries between different deformation mechanisms of the TNZx alloys. In Fig. 9, the regions of α, α + β and β phases and their possible deformation mechanisms (i.e. slip and twin) can be clearly seen. The phase stability in $\overline{Bo}$-$\overline{Md}$ map can be observed by plotting the $\overline{Bo}$ and $\overline{Md}$ values of the TNZx alloys in the $\overline{Bo}$-$\overline{Md}$ map as suggested by Ref. [27]. It is reported that alloy should have high $\overline{Bo}$ and low $\overline{Md}$ values to attain a high β stability position in the $\overline{Bo}$-$\overline{Md}$ map [8]. The locations of all the studied alloys, on the basis of their respective $\overline{Bo}$ and $\overline{Md}$ values presented in Table 1, are plotted in the $\overline{Bo}$-$\overline{Md}$ map. It is clearly observed from Fig. 9 that TNZ0 is located in the martensite region, TNZ2 is placed in the

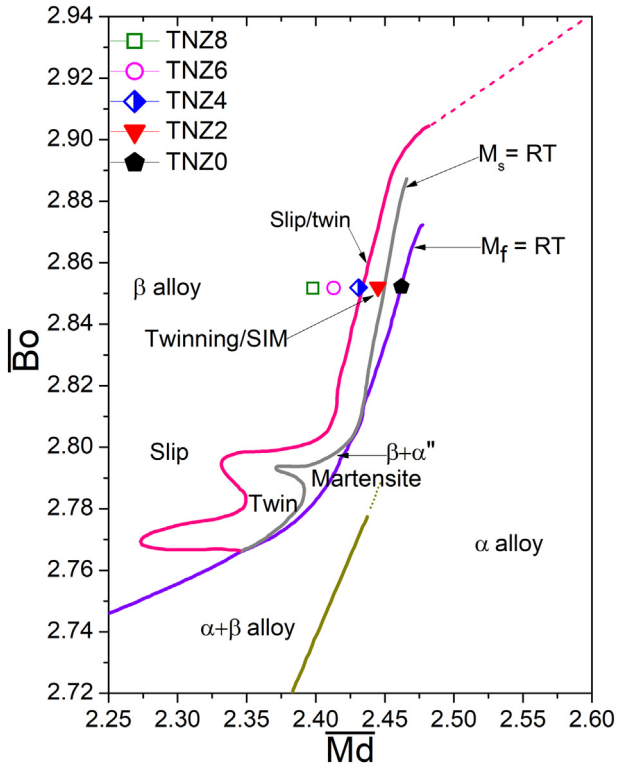

Fig. 9. The locations of the Ti-25Nb-8Zr-xCr alloys (name of the alloys are shortened as TNZx) on the phase stability diagram.

twin region, TNZ4 is almost on the boundary of slip/twin, while the rest alloys (i.e. TNZ6 and TNZ8) are located in the slip region. Deformation mechanisms can also be estimated by plotting the $\overline{e/a}$ and $\overline{\Delta r}$ values of the studied alloys in $\overline{e/a}$-$\overline{\Delta r}$ diagram as suggested by Ref. [19].

In this work, the values of $\overline{e/a}$ and $\overline{\Delta r}$ (Table 1) for all the TNZx alloys and some other studied Ti alloys in literature are plotted in Fig. 10 in order to investigate the deformation mechanism through $\overline{e/a}$-$\overline{\Delta r}$ diagram. All the plotted alloys are in good agreement with the predicted deformation mechanisms as suggested by $\overline{e/a}$-$\overline{\Delta r}$ diagram. Fig. 10 predicts the twin or SIM mechanism for TNZ2 and TNZ0, slip + twin mechanism for TNZ4 and slip mechanism for TNZ6 and TNZ8. Furthermore,

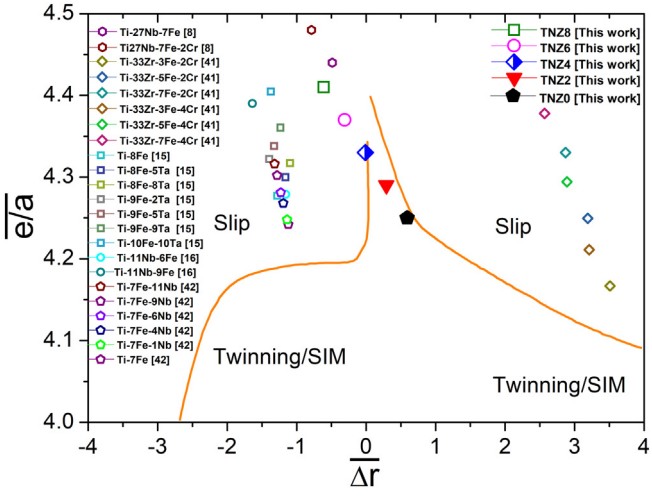

Fig. 10. The locations of the Ti-25Nb-8Zr-xCr alloys (name of the alloys are shortened as TNZx) on the $\overline{e/a}$ -$\overline{\Delta r}$ diagram. The orange lines in this diagram are plotted based on Ref. [19].

Kolli et al. [63] studied the influence of the values of Mo_{eq} on the various deformation mechanisms for Ti alloys and found that the deformation mechanisms change in the sequence of $\alpha' \rightarrow \alpha'' \rightarrow \omega$ + twinning $\rightarrow$ twinning + Slip $\rightarrow$ Slip as increasing the values of Mo_{eq} [63]. The values of Mo_{eq} for the studied TNZx alloys (as shown in Table 1) suggest the similar trend as suggested by Ref. [63]. As a result, the deformation mechanisms predicted by the $\overline{Bo}$-$\overline{Md}$ diagram and $\overline{e/a}$-$\overline{\Delta r}$ diagram are in good agreement with that by morphologies of deformation bands around the micro-hardness indentations for the studied TNZx alloys.

3.4. Fracture analyses

It is known that shear bands are the localization of high shear strains which cause the occurrence of deformation bands along the direction of maximum shear stress [64]. Prior to the formation of shear bands, a material typically experiences a yielding and deformation twinning followed by plastic deformation [65]. Thus, analyses of shear bands were performed on the samples prepared metallographically for the investigated Cr-containing Ti alloys at the same load limit (at 100 kN). The features of these analyses are presented in Fig. 11. TNZ0 is not included in this analysis as the TNZ0 fails before reaching the 100 kN in compression testing. Hence, for analyzing the shear bands at the same load limit, the compression tests were stopped at 100 kN in the present work. Shear bands can be clearly noticed in Fig. 11a–d. In Fig. 11b, thick shear bands can be observed in TNZ4, which indicates that a large plastic deformation occurs in TNZ4 alloy and as a consequence TNZ4 relatively displays the largest plastic strain [41,66].

Fig. 12 shows the SEM images of fractographic morphologies captured on the deformed outer surfaces of the tested specimens for the investigated TNZx alloys. The shear crack angle between the fracture plane and compressive loading direction is almost 45° which indicates that cracks form in a shear mode [16]. There is a minor shear crack on the outer surfaces of the Cr-containing alloys. Fig. 12 shows the SEM fractographic images for the deformed Cr-containing TNZx alloys together with TNZ0. Fig. 12a displays the flat main fracture in TNZ0 which demonstrates a transgranular fracture. Further, the cracks can be observed on the fractographic image of TNZ0. On the other hand, Fig. 12b–e displays that the fracture is not observed in the deformed samples of all the investigated Cr-containing TNZx alloys since these alloys do not fail in mechanical compression testing. Nonetheless, many shear bands are observed in all the deformed Cr-containing TNZx alloys. Therefore, all of the investigated Cr-containing TNZx alloys possess a significantly large plasticity. The fractographic results are in line with the studied mechanical properties of TNZx alloys.

4. Conclusions

The present work investigates the microstructural characteristics, the mechanical properties, the elasto-plastic deformation and deformation behaviors for the newly-designed Ti-25Nb-8Zr-xCr (x = 0, 2, 4, 6, 8 wt%) alloys, which were designed based on DV-Xα cluster method and $\overline{e/a}$-$\overline{\Delta r}$ diagram. The following concluding remarks can be made from the results presented.

- The Ti-25Nb-8Zr alloy displays a dual-phase (bcc β and orthorhombic α" phases) microstructure while the Cr-containing Ti-25Nb-8Zr-xCr alloys predominantly comprise a single bcc β phase in microstructure.
- All the Cr-containing alloys do not fail in the compression tests performed up to the load capacity at 100 kN. All the Cr-containing alloys exhibit impressive maximum compressive strength (~4.5 GPa) and superior plastic strain (~75%). Both hardness (1.91 GPa to 2.63 GPa) and yield strength (382 MPa to 773 MPa) increase as the Cr concentration increases in the Ti-25Nb-8Zr-xCr alloys. Enhanced strain hardening rate (5 GPa) is achieved in Ti-25Nb-8Zr-2Cr alloy.
- The predicted deformation mechanisms based on deformation bands investigated around micro-hardness indentations, $\overline{Bo}$-$\overline{Md}$ diagram and

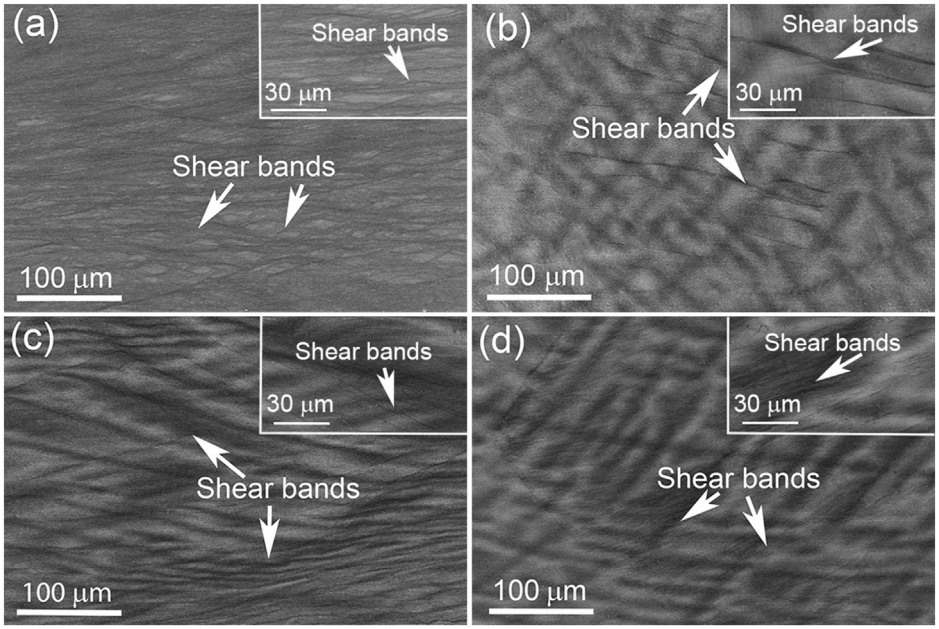

Fig. 11. Backscattered SEM images of mechanically deformed surface morphologies of the Ti-25Nb-8Zr-xCr alloys containing Cr: (a) TNZ2, (b) TNZ4, (c) TNZ6 and (d) TNZ8.

$\overline{e/a}$-$\overline{\Delta r}$ diagram are in line with each other for the investigated Ti-25Nb-8Zr-xCr alloys. Moreover, the results of the fracture analyses and the mechanical properties for the investigated alloys are also in good agreement with each other.

- Among all the as-cast alloys, the Ti-25Nb-8Zr-2Cr and Ti-25Nb-8Zr-4Cr alloys exhibit significant strain hardening and superior plasticity.

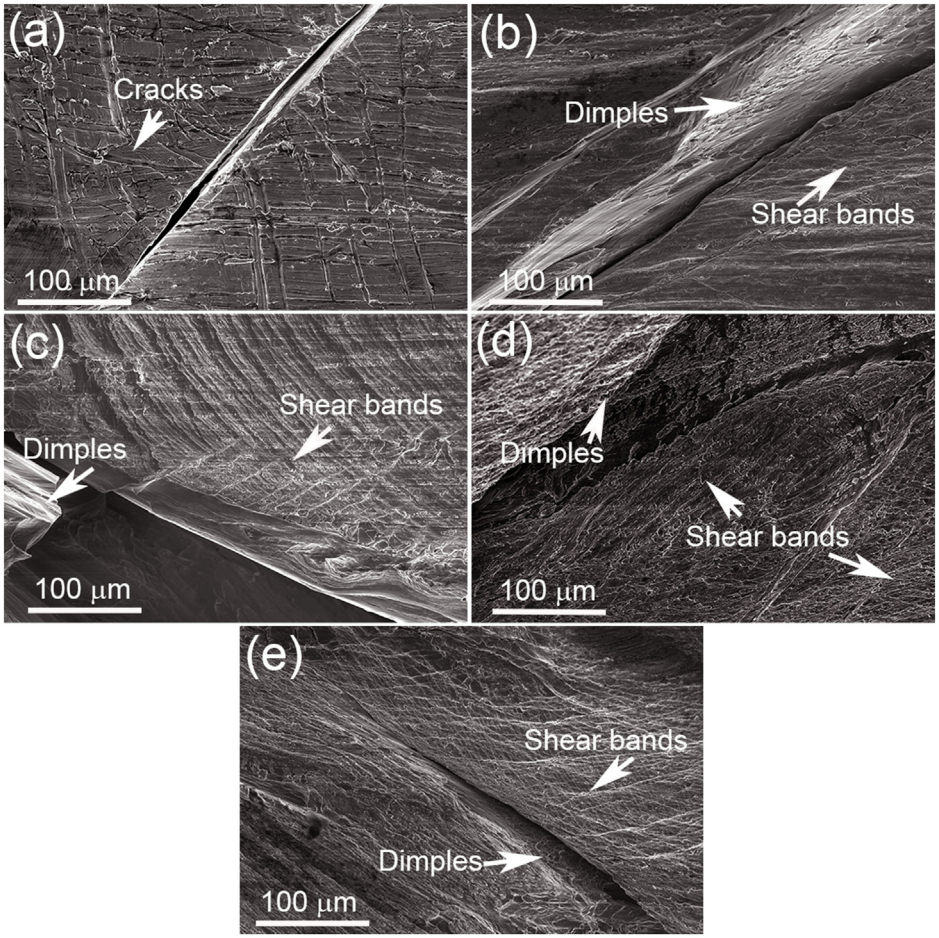

Fig. 12. SEM fracture surface morphologies of the Ti-25Nb-8Zr-xCr alloys: (a) TNZ0, (b) TNZ2, (c) TNZ4, (d) TNZ6 and (e) TNZ8.

Both alloys can be potentially used in advanced biomedical and structural applications.

Acknowledgements

The authors would like to acknowledge the financial supports provided by National Science Foundation under Grant No. 51674167 and Fundamental Research Funds for the Central Universities under Grant No. YG2017ZD06. S.F. Jawed and C.D. Rabadia are grateful for the financial support from the ECU-HEC Joint Scholarship and ECU Postgraduate Research Scholarship, respectively.

CRediT authorship contribution statement

S.F. Jawed: Conceptualization, Methodology, Investigation, Writing - original draft, Writing - review & editing. **C.D. Rabadia**: Investigation, Writing - review & editing. **Y.J. Liu**: Investigation, Writing - review & editing. **L.Q. Wang**: Investigation. **Y.H. Li**: Writing - review & editing. **X.H. Zhang**: Writing - review & editing. **L.C. Zhang**: Conceptualization, Methodology, Investigation, Writing - original draft, Writing - review & editing, Supervision.

Data availability statement

The raw/processed data required to reproduce these findings cannot be shared at this time as the data also forms part of an ongoing study.

References

[1] Y.J. Liu, S.J. Li, L.C. Zhang, Y.L. Hao, T.B. Sercombe, Early plastic deformation behaviour and energy absorption in porous β-type biomedical titanium produced by selective laser melting, Scripta Mater 153 (2018) 99–103, https://doi.org/10.1016/j.scriptamat.2018.05.010.
[2] Y. Chen, J. Zhang, N. Dai, P. Qin, H. Attar, L.-C. Zhang, Corrosion behaviour of selective laser melted Ti-TiB biocomposite in simulated body fluid, Electrochim. Acta 232 (2017) 89–97, https://doi.org/10.1016/j.electacta.2017.02.112.
[3] L.-C. Zhang, Y. Liu, S. Li, Y. Hao, Additive manufacturing of titanium alloys by electron beam melting: a review, Adv. Eng. Mater. 20 (2018), 1700842. https://doi.org/10.1002/adem.201700842.
[4] M. Marteleur, F. Sun, T. Gloriant, P. Vermaut, P.J. Jacques, F. Prima, On the design of new β-metastable titanium alloys with improved work hardening rate thanks to simultaneous TRIP and TWIP effects, Scripta Mater 66 (2012) 749–752, https://doi.org/10.1016/j.scriptamat.2012.01.049.
[5] L. Wang, L. Xie, Y. Lv, L.-C. Zhang, L. Chen, Q. Meng, J. Qu, D. Zhang, W. Lu, Microstructure evolution and superelastic behavior in Ti-35Nb-2Ta-3Zr alloy processed by friction stir processing, Acta Mater. 131 (2017) 499–510, https://doi.org/10.1016/j.actamat.2017.03.079.
[6] C.D. Rabadia, Y.J. Liu, L.Y. Chen, S.F. Jawed, L.Q. Wang, H. Sun, L.C. Zhang, Deformation and strength characteristics of laves phases in titanium alloys, Mater. Des. 179 (2019), 107891. https://doi.org/10.1016/j.matdes.2019.107891.
[7] L.C. Zhang, L.Y. Chen, A review on biomedical titanium alloys: recent progress and prospect, Adv. Eng. Mater. 21 (2019), 1801215. https://doi.org/10.1002/adem.201801215.
[8] C.D. Rabadia, Y.J. Liu, G.H. Cao, Y.H. Li, C.W. Zhang, T.B. Sercombe, H. Sun, L.C. Zhang, High-strength β stabilized Ti-Nb-Fe-Cr alloys with large plasticity, Mater. Sci. Eng. A 732 (2018) 368–377, https://doi.org/10.1016/j.msea.2018.07.031.
[9] Y.J. Liu, H.L. Wang, S.J. Li, S.G. Wang, W.J. Wang, W.T. Hou, Y.L. Hao, R. Yang, L. Zhang, Compressive and fatigue behavior of beta-type titanium porous structures fabricated by electron beam melting, Acta Mater. 126 (2017) 58–66, https://doi.org/10.1016/j.actamat.2016.12.052.
[10] S. Acharya, A.G. Panicker, D.V. Laxmi, S. Suwas, K. Chatterjee, Study of the influence of Zr on the mechanical properties and functional response of Ti-Nb-Ta-Zr-O alloy for orthopedic applications, Mater. Des. 164 (2019), 107555. https://doi.org/10.1016/j.matdes.2018.107555.
[11] A. Biesiekierski, J. Lin, Y. Li, D. Ping, Y. Yamabe-Mitarai, C. Wen, Investigations into Ti–(Nb, Ta)–Fe alloys for biomedical applications, Acta Biomater. 32 (2016) 336–347, https://doi.org/10.1016/j.actbio.2015.12.010.
[12] S. Ozan, J. Lin, Y. Li, R. Ipek, C. Wen, Development of Ti–Nb–Zr alloys with high elastic admissible strain for temporary orthopedic devices, Acta Biomater. 20 (2015) 176–187, https://doi.org/10.1016/j.actbio.2015.03.023.
[13] Y. Liu, S. Li, W. Hou, S. Wang, Y. Hao, R. Yang, T.B. Sercombe, L.-C. Zhang, Electron beam melted beta-type Ti–24Nb–4Zr–8Sn porous structures with high strength-to-modulus ratio, J. Mater. Sci. Technol. 32 (2016) 505–508, https://doi.org/10.1016/j.jmst.2016.03.020.
[14] N. Hafeez, S. Liu, E. Lu, L. Wang, R. Liu, W. lu, L.-C. Zhang, Mechanical behavior and phase transformation of β-type Ti-35Nb-2Ta-3Zr alloy fabricated by 3D-printing, J. Alloys Compd. 790 (2019) 117–126, https://doi.org/10.1016/j.jallcom.2019.03.138.
[15] S. Ehtemam-Haghighi, H.B. Lu, G.Y. Jian, G.H. Cao, D. Habibi, L.C. Zhang, Effect of α″martensite on the microstructure and mechanical properties of beta-type Ti–Fe–Ta alloys, Mater. Des. 76 (2015) 47–54, https://doi.org/10.1016/j.matdes.2015.03.028.
[16] S. Ehtemam-Haghighi, Y.J. Liu, G.H. Cao, L.C. Zhang, Phase transition, microstructural evolution and mechanical properties of Ti-Nb-Fe alloys induced by Fe addition, Mater. Des. 97 (2016) 279–286, https://doi.org/10.1016/j.matdes.2016.02.094.
[17] F. Sun, J.Y. Zhang, M. Marteleur, C. Brozek, E.F. Rauch, M. Veron, P. Vermaut, P.J. Jacques, F. Prima, A new titanium alloy with a combination of high strength, high strain hardening and improved ductility, Scripta Mater 94 (2015) 17–20, https://doi.org/10.1016/j.scriptamat.2014.09.005.
[18] W. Zhu, J. Lei, C. Tan, Q. Sun, W. Chen, L. Xiao, J. Sun, A novel high-strength β-Ti alloy with hierarchical distribution of α-phase: the superior combination of strength and ductility, Mater. Des. 168 (2019), 107640. https://doi.org/10.1016/j.matdes.2019.107640.
[19] C.H. Wang, A.M. Russell, G.H. Cao, A semi-empirical approach to the prediction of deformation behaviors of β-Ti alloys, Scripta Mater 158 (2019) 62–65, https://doi.org/10.1016/j.scriptamat.2018.08.035.
[20] Y.J. Liu, Y.S. Zhang, L. Zhang, Transformation-induced plasticity and high strength in beta titanium alloy manufactured by selective laser melting, Materialia 6 (2019), 100299. https://doi.org/10.1016/j.mtla.2019.100299.
[21] R. Karre, M.K. Niranjan, S.R. Dey, First principles theoretical investigations of low Young's modulus beta Ti–Nb and Ti–Nb–Zr alloys compositions for biomedical applications, Mater. Sci. Eng. C 50 (2015) 52–58, https://doi.org/10.1016/j.msec.2015.01.061.
[22] F.A. Shah, M. Trobos, P. Thomsen, A. Palmquist, Commercially pure titanium (cp-Ti) versus titanium alloy (Ti6Al4V) materials as bone anchored implants—is one truly better than the other? Mater. Sci. Eng. C 62 (2016) 960–966, https://doi.org/10.1016/j.msec.2016.01.032.
[23] F. Sun, J.Y. Zhang, M. Marteleur, T. Gloriant, P. Vermaut, D. Laillé, P. Castany, C. Curfs, P.J. Jacques, F. Prima, Investigation of early stage deformation mechanisms in a metastable β titanium alloy showing combined twinning-induced plasticity and transformation-induced plasticity effects, Acta Mater. 61 (2013) 6406–6417, https://doi.org/10.1016/j.actamat.2013.07.019.
[24] F. Sun, J.Y. Zhang, C. Brozek, M. Marteleur, M. Veron, E. Rauch, T. Gloriant, P. Vermaut, C. Curfs, P.J. Jacques, F. Prima, The role of stress induced martensite in ductile metastable beta Ti-alloys showing combined TRIP/TWIP effects, Mater. Today: Proc. 2 (2015) S505–S510, https://doi.org/10.1016/j.matpr.2015.07.336.
[25] L.H. Liu, C. Yang, F. Wang, S.G. Qu, X.Q. Li, W.W. Zhang, Y.Y. Li, L. Zhang, Ultrafine grained Ti-based composites with ultrahigh strength and ductility achieved by equiaxing microstructure, Mater. Des. 79 (2015) 1–5, https://doi.org/10.1016/j.matdes.2015.04.032.
[26] M. Morinaga, M. Kato, T. Kamimura, M. Fukumoto, I. Harada, K. Kubo, Theoretical design of b-type titanium alloys, tinanium'92, science and technology, in: F.H. Froes, I.L. Caplan (Eds.),Proc. 7th Int. Conf. on Titanium, San Diego, California, USA 1993, pp. 276–283.
[27] M. Abdel-Hady, K. Hinoshita, M. Morinaga, General approach to phase stability and elastic properties of β-type Ti-alloys using electronic parameters, Scripta Mater 55 (2006) 477–480, https://doi.org/10.1016/j.scriptamat.2006.04.022.
[28] D. Kuroda, M. Niinomi, M. Morinaga, Y. Kato, T. Yashiro, Design and mechanical properties of new β type titanium alloys for implant materials, Mater. Sci. Eng. A 243 (1998) 244–249, https://doi.org/10.1016/S0921-5093(97)00808-3.
[29] S.F. Jawed, C.D. Rabadia, Y.J. Liu, L.Q. Wang, Y.H. Li, X.H. Zhang, L.C. Zhang, Mechanical characterization and deformation behavior of β-stabilized Ti-Nb-Sn-Cr alloys, J. Alloys Compd. 792 (2019) 684–693, https://doi.org/10.1016/j.jallcom.2019.04.079.
[30] Q. Wang, C. Han, T. Choma, Q. Wei, C. Yan, B. Song, Y. Shi, Effect of Nb content on microstructure, property and in vitro apatite-forming capability of Ti-Nb alloys fabricated via selective laser melting, Mater. Des. 126 (2017) 268–277, https://doi.org/10.1016/j.matdes.2017.04.026.
[31] K. Endoh, M. Tahara, T. Inamura, H. Hosoda, Effect of Sn and Zr content on superelastic properties of Ti-Mo-Sn-Zr biomedical alloys, Mater. Sci. Eng. A 704 (2017) 72–76, https://doi.org/10.1016/j.msea.2017.07.097.
[32] J. Málek, F. Hnilica, J. Veselý, B. Smola, K. Kolařík, J. Fojt, M. Vlach, V. Kodetová, The effect of Zr on the microstructure and properties of Ti-35Nb-XZr alloy, Mater. Sci. Eng. A 675 (2016) 1–10, https://doi.org/10.1016/j.msea.2016.07.069.
[33] J.C. Williams, B.S. Hickman, D.H. Leslie, The effect of ternary additions on the decomposition of metastable beta-phase titanium alloys, Metallurgical Transactions 2 (1971) 477–484, https://doi.org/10.1007/bf02663337.
[34] H.-C. Hsu, S.-C. Wu, S.-K. Hsu, T.-F. Lin, W.-F. Ho, Structure and mechanical properties of as-cast Ti–5Nb–xCr alloys, Mater. Des. 51 (2013) 268–273, https://doi.org/10.1016/j.matdes.2013.04.001.
[35] P. Wang, Y. Feng, F. Liu, L. Wu, S. Guan, Microstructure and mechanical properties of Ti–Zr–Cr biomedical alloys, Mater. Sci. Eng. C 51 (2015) 148–152, https://doi.org/10.1016/j.msec.2015.02.028.
[36] J. Gao, Y. Huang, D. Guan, A.J. Knowles, L. Ma, D. Dye, W.M. Rainforth, Deformation mechanisms in a metastable beta titanium twinning induced plasticity alloy with high yield strength and high strain hardening rate, Acta Mater. 152 (2018) 301–314, https://doi.org/10.1016/j.actamat.2018.04.035.
[37] Q. Li, M. Niinomi, J. Hieda, M. Nakai, K. Cho, Deformation-induced ω phase in modified Ti–29Nb–13Ta–4.6 Zr alloy by Cr addition, Acta Biomater. 9 (2013) 8027–8035, https://doi.org/10.1016/j.actbio.2013.04.032.
[38] S. Sadeghpour, S. Abbasi, M. Morakabati, A. Kisko, L. Karjalainen, D. Porter, On the compressive deformation behavior of new beta titanium alloys designed by d-electron method, J. Alloys Compd. 746 (2018) 206–217, https://doi.org/10.1016/j.jallcom.2018.02.212.

[39] M. Morinaga, 1.3 - The molecular orbital approach and its application to biomedical titanium alloy design, in: F.H. Froes, M. Qian (Eds.), Titanium in Medical and Dental Applications, Woodhead Publishing 2018, pp. 39–64.
[40] A. Biesiekierski, J. Wang, M.A.-H. Gepreel, C. Wen, A new look at biomedical Ti-based shape memory alloys, Acta Biomater. 8 (2012) 1661–1669, https://doi.org/10.1016/j.actbio.2012.01.018.
[41] C.D. Rabadia, Y.J. Liu, L. Wang, H. Sun, L.C. Zhang, Laves phase precipitation in Ti-Zr-Fe-Cr alloys with high strength and large plasticity, Mater. Des. 154 (2018) 228–238, https://doi.org/10.1016/j.matdes.2018.05.035.
[42] S. Ehtemam-Haghighi, Y.J. Liu, G.H. Cao, L.C. Zhang, Influence of Nb on the β → α″ martensitic phase transformation and properties of the newly designed Ti–Fe–Nb alloys, Mater. Sci. Eng. C 60 (2016) 503–510, https://doi.org/10.1016/j.msec.2015.11.072.
[43] J. Chakrabarty, Applied Plasticity, second ed. Springer-Verlag, USA, 2000.
[44] C. Brozek, F. Sun, P. Vermaut, Y. Millet, A. Lenain, D. Embury, P.J. Jacques, F. Prima, A β-titanium alloy with extra high strain-hardening rate: design and mechanical properties, Scripta Mater 114 (2016) 60–64, https://doi.org/10.1016/j.scriptamat.2015.11.020.
[45] D.R.N. Correa, F.B. Vicente, T.A.G. Donato, V.E. Arana-Chavez, M.A.R. Buzalaf, C.R. Grandini, The effect of the solute on the structure, selected mechanical properties, and biocompatibility of Ti–Zr system alloys for dental applications, Mater. Sci. Eng. C 34 (2014) 354–359, https://doi.org/10.1016/j.msec.2013.09.032.
[46] S. Liang, X. Feng, L. Yin, X. Liu, M. Ma, R. Liu, Development of a new β Ti alloy with low modulus and favorable plasticity for implant material, Mater. Sci. Eng. C 61 (2016) 338–343, https://doi.org/10.1016/j.msec.2015.12.076.
[47] Y.L. Zhou, M. Niinomi, T. Akahori, Effects of Ta content on Young's modulus and tensile properties of binary Ti–Ta alloys for biomedical applications, Mater. Sci. Eng. A 371 (2004) 283–290, https://doi.org/10.1016/j.msea.2003.12.011.
[48] W.-F. Ho, S.-C. Wu, S.-K. Hsu, Y.-C. Li, H.-C. Hsu, Effects of molybdenum content on the structure and mechanical properties of as-cast Ti–10Zr-based alloys for biomedical applications, Mater. Sci. Eng. C 32 (2012) 517–522, https://doi.org/10.1016/j.msec.2011.12.003.
[49] D.J. Lin, J.H. Chern Lin, C.P. Ju, Structure and properties of Ti–7.5Mo–xFe alloys, Biomater 23 (2002) 1723–1730, https://doi.org/10.1016/S0142-9612(01)00233-2.
[50] Y. Kusano, T. Inamura, H. Kanetaka, S. Miyazaki, H. Hosoda, Phase constitution and mechanical properties of Ti-(Cr, Mn)-Sn biomedical alloys, Mater. Sci. Forum 654-656 (2010) 2118–2121, https://doi.org/10.4028/www.scientific.net/MSF.654-656.2118.
[51] S.-P. Wang, J. Xu, TiZrNbTaMo high-entropy alloy designed for orthopedic implants: as-cast microstructure and mechanical properties, Mater. Sci. Eng. C 73 (2017) 80–89, https://doi.org/10.1016/j.msec.2016.12.057.
[52] L.C. Zhang, J. Das, H.B. Lu, C. Duhamel, M. Calin, J. Eckert, High strength Ti–Fe–Sn ultrafine composites with large plasticity, Scripta Mater 57 (2007) 101–104, https://doi.org/10.1016/j.scriptamat.2007.03.031.
[53] P. Zhang, S.X. Li, Z.F. Zhang, General relationship between strength and hardness, Mater. Sci. Eng. A 529 (2011) 62–73, https://doi.org/10.1016/j.msea.2011.08.061.
[54] J.S. Keist, T.A. Palmer, Development of strength-hardness relationships in additively manufactured titanium alloys, Mater. Sci. Eng. A 693 (2017) 214–224, https://doi.org/10.1016/j.msea.2017.03.102.
[55] C.D. Rabadia, Y.J. Liu, S.F. Jawed, L. Wang, Y.H. Li, X.H. Zhang, T.B. Sercombe, H. Sun, L.C. Zhang, Improved deformation behavior in Ti-Zr-Fe-Mn alloys comprising the C14 type laves and β phases, Mater. Des. 160 (2018) 1059–1070, https://doi.org/10.1016/j.matdes.2018.10.049.
[56] Y. Yang, S. Wu, G. Li, Y. Li, Y. Lu, K. Yang, P. Ge, Evolution of deformation mechanisms of Ti–22.4 Nb–0.73 Ta–2Zr–1.34O alloy during straining, Acta Mater. 58 (2010) 2778–2787, https://doi.org/10.1016/j.actamat.2010.01.015.
[57] M.J. Lai, T. Li, D. Raabe, ω phase acts as a switch between dislocation channeling and joint twinning- and transformation-induced plasticity in a metastable β titanium alloy, Acta Mater. 151 (2018) 67–77, https://doi.org/10.1016/j.actamat.2018.03.053.
[58] I. Gutierrez-Urrutia, D. Raabe, Dislocation and twin substructure evolution during strain hardening of an Fe–22 wt% Mn–0.6 wt% C TWIP steel observed by electron channeling contrast imaging, Acta Mater. 59 (2011) 6449–6462, https://doi.org/10.1016/j.actamat.2011.07.009.
[59] K.K. Chawla, M. Meyers, Mechanical Behavior of Materials, second ed. Prentice Hall, Up. Saddle River, 1999.
[60] Y.L. Hao, S.J. Li, S.Y. Sun, C.Y. Zheng, Q.M. Hu, R. Yang, Super-elastic titanium alloy with unstable plastic deformation, Appl. Phys. Lett. 87 (2005), 091906. https://doi.org/10.1063/1.2037192.
[61] M.J. Lai, C.C. Tasan, D. Raabe, On the mechanism of {332} twinning in metastable β titanium alloys, Acta Mater. 111 (2016) 173–186, https://doi.org/10.1016/j.actamat.2016.03.040.
[62] U. Ramamurty, S. Jana, Y. Kawamura, K. Chattopadhyay, Hardness and plastic deformation in a bulk metallic glass, Acta Mater. 53 (2005) 705–717, https://doi.org/10.1016/j.actamat.2004.10.023.
[63] R.P. Kolli, W.J. Joost, S. Ankem, Phase stability and stress-induced transformations in beta titanium alloys, JOM 67 (2015) 1273–1280, https://doi.org/10.1007/s11837-015-1411-y.
[64] A.L. Greer, Y.Q. Cheng, E. Ma, Shear bands in metallic glasses, Mater. Sci. Eng. R 74 (2013) 71–132, https://doi.org/10.1016/j.mser.2013.04.001.
[65] M.A. Meyers, G. Subhash, B.K. Kad, L. Prasad, Evolution of microstructure and shear-band formation in α-hcp titanium, Mech. Mater. 17 (1994) 175–193, https://doi.org/10.1016/0167-6636(94)90058-2.
[66] Y. Yang, X.M. Li, X.L. Tong, Q.M. Zhang, C.Y. Xu, Effects of microstructure on the adiabatic shearing behaviors of titanium alloy, Mater. Sci. Eng. A 528 (2011) 3130–3133, https://doi.org/10.1016/j.msea.2010.12.068.